Journal of Power Sources 625 (2025) 235626

Contents lists available at ScienceDirect

Journal of Power Sources

journal homepage: www.elsevier.com/locate/jpowsour

In-situ TEM reduction of a solid oxide cell with NiO/YSZ fuel electrode

S. Korneychuk [a,b,c,*], C. Grosselindemann [d], N.H. Menzler [e], A. Weber [d], A. Pundt [a]

[a] IAM-WK, Karlsruhe Institute of Technology, Karlsruhe, Germany
[b] INT, Karlsruhe Institute of Technology, Karlsruhe, Germany
[c] KNMFi, Karlsruhe Institute of Technology, Karlsruhe, Germany
[d] IAM-ET, Karlsruhe Institute of Technology, Karlsruhe, Germany
[e] Forschungszentrum Jülich GmbH, Institute of Energy Materials and Devices (IMD), IMD-2: Materials Synthesis and Processing, Jülich, Germany

HIGHLIGHTS

- Real-time observation of NiO/YSZ reduction for the SOC electrode with *in-situ* TEM
- High initial reduction temperature lead to the better quality of TPBs
- NiO/YSZ reduces at triple junctions and phase boundaries at low temperatures
- Low initial reduction temperatures decrease the connection between Ni and YSZ
- *In-situ* reduction in TEM compared to the *ex-situ* reduction of the bulk SOC

GRAPHICAL ABSTRACT

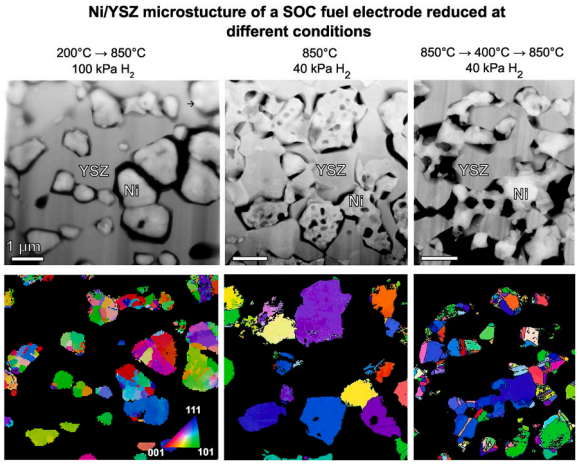

ABSTRACT

Ni/YSZ fuel cell electrodes of high-temperature solid oxide cells are commonly reduced from NiO/YSZ under hydrogen atmosphere at high temperatures, prior to operation. Ni provides the required electronic conductivity and electrocatalytic activity and thus enables operability of the cell. The reduction results in a significant change in microstructure which can be observed by *in-situ* transmission electron microscopy. As specific microstructural properties are crucial to achieve high performance and durability of the cell, a comprehensive understanding of the reduction process is required. In this contribution, an *in-situ* real-time observation of microstructural changes during reduction of a NiO/YSZ-compound as well as pure NiO-samples is performed and compared to an *ex-situ* analysis of a corresponding cell after the reduction. For the first time, we reduce NiO/YSZ with *in-situ* TEM at H_2 pressures up to 1 atm and different temperatures up to 850 °C, relevant to the actual reduction conditions of the fuel electrodes. With three different reduction schemes, we show a drastic influence of the reduction conditions on Ni microstructure and Ni/YSZ interface. At low temperatures, grain boundaries and triple junctions between NiO and YSZ are determined as the starting points of the reduction process. This process reduces the connection between Ni and YSZ. Novel *in-situ* TEM results from this work provide a clear evidence at the nanoscale that high initial reduction temperatures lead to the different microstructure of Ni, better connection between Ni grains and superior quality of Ni/YSZ interface. This is crucial to achieve a larger number of electrochemically active triple phase boundaries between Ni/YSZ and gas.

* Corresponding author. IAM-WK, Karlsruhe Institute of Technology, Karlsruhe, Germany.
E-mail address: svetlana.korneychuk@kit.edu (S. Korneychuk).

https://doi.org/10.1016/j.jpowsour.2024.235626
Received 2 August 2024; Received in revised form 20 September 2024; Accepted 15 October 2024
Available online 29 October 2024
0378-7753/© 2024 The Authors. Published by Elsevier B.V. This is an open access article under the CC BY license (http://creativecommons.org/licenses/by/4.0/).

1. Introduction

Solid oxide cells (SOCs) play a key role in the transition to the green economy. They are able to convert the chemical energy of a fuel into electricity (fuel cell mode) and vice versa electrical energy into hydrogen or syngas (electrolyzer mode). SOCs are commonly operated at high temperatures of 600–900 °C at a gas pressure of 100 kPa (atmospheric pressure). In most SOCs the porous fuel electrode consists of an ion conducting ceramic phase like yttria-stabilized zirconia (YSZ) and a metallic, electron conducting phase of Ni, which also works as electrocatalyst, named cermet. The electrochemical reaction in such an electrode is located at the triple phase boundary (TPB) between Ni, YSZ and a pore or at the vicinity of TPB [1]. To enable a high performance, Ni, YSZ- and the pore-phase have to form continuous matrices to enable the transport of electrons, oxygen ions and gaseous species to/from the TPBs.

During the initial operation of a solid oxide cell (SOC), a pre-defined start-up procedure has to be followed prior to regular operation [2,3]. For solid oxide cells with nickel-based fuel electrodes this includes the reduction of nickel oxide (NiO) to metallic nickel (Ni). Nickel oxide is chosen within the manufacturing process of the cell as more complex steps as sintering under vacuum or reducing conditions can be avoided [4–6]. However, the reduction of NiO to Ni results in a significant change of microstructure and the volume fractions, namely an increase of the pore volume fraction and a decrease of the Ni-related volume fraction [7,8]. Microstructural parameters, directly correlating with the electrochemical performance of the electrode, such as porosity, tortuosity and the density of electrochemically active triple phase boundaries (Ni/YSZ/gas-phase) are affected by the reduction procedure [9–16]. The resulting microstructure will determine performance and durability of the cell [17–21].

Reduction of pure NiO in hydrogen has been excessively studied in literature and can be described by the simple equation: $NiO + H_2 = Ni + H_2O$. According to Richardson et al. [22] and previous works [23,24], this reaction can be separated in five stages: 1) H_2 molecule dissociation on NiO or later, on Ni; 2) diffusion of H atoms to the reaction center; 3) breakage of Ni-O bonds to form Ni^0 atoms; 4) nucleation of Ni^0 atoms into metallic clusters and 5) further growth of nickel metal clusters. When first Ni^0 clusters are formed the reaction proceeds autocatalytically. Overall, the reduction process of NiO can be described with the Johnson–Mehl-Avrami-Kolmogorov (JMAK) nucleation model [25–27].

However, the size and shape of initial NiO material, reduction temperature and heating rate together with hydrogen pressure can influence each of the stages above and, therefore, have a strong impact on the reaction speed and final Ni morphology. For example, Manukyan et al. [28] showed that the reduction of polycrystalline NiO with a grain size of 1–3 μm at low temperatures (270–500 °C) results in porous polycrystalline regions of Ni-NiO within the original NiO grains. Ni reduced at high temperatures above 900 °C preserves the crystallographic structure of the original NiO grains. The authors attributed this difference to the higher amount of Ni nuclei, faster nucleation and growth of Ni at high temperatures preserving the initial NiO crystallinity. Lee et al. [29] showed that larger NiO powder with average 150 μm particle size reduces slower than the smaller one of 0.05 μm at the same conditions. Richardson et al. [22] demonstrated that faster heating rate decreases the duration of the initial nucleation stage leading to the lower reduction temperatures. It was suggested by Bandrowski et al. [30] that kinetics of the early stage of reduction involving reaction of NiO with hydrogen atoms absorbed at the surface, is proportional to the square root of the hydrogen partial pressure. During later stages of reduction, hydrogen pressure in a range of a few thousands Pa does not play a significant role in the final Ni morphology leading mostly to the polycrystalline Ni [28]. However, reduction of the ultrathin NiO film at very low hydrogen pressures of about 10^{-5} Pa result in single crystalline Ni surface [31]. Preservation of initial NiO crystallinity in final Ni/YSZ structures reduced at about 140 Pa, was also observed by Jeangros [32].

Such strong dependence of Ni morphology on the reduction parameters asks for close replication of NiO/YSZ reduction conditions in our experiment. Transmission electron microscopy (TEM) is a powerful tool to investigate the microstructure of solid oxide cells [33,34]. So far, knowledge about the physical mechanisms behind the microstructural changes is still limited and requires a need for in-operando investigation [33]. The reduction of NiO/YSZ was studied with environmental TEM (ETEM) at initial moderate reduction temperatures of 200–500 °C and hydrogen pressures of about 150 Pa in a range of works. Simonsen et al. [35,36] found that reduction of NiO start between 300 and 400 °C and YSZ has an inhibiting effect on NiO reduction. The authors also observed the coarsening on Ni grains at higher temperatures. In a set of works by Faes et al. [37] and Jeangros [32,38] in ETEM, the authors observed the start reduction of at 320 °C at the NiO/YSZ interface. With the temperature increase the reduction is initiated also from the free surface of NiO grains. The authors suggested [32] that the reduction process at the Ni/YSZ interface is activated by oxygen transferring from NiO to YSZ resulting in NiO oxygen vacancies and thus creating hydrogen adsorption sites. The role of NiO/NiO grain boundaries is further discussed in Ref. [38], concluding that coherent grain boundaries lead to preservation of the contact between these grains during the reduction. Incoherent grain boundaries result in separation of the grains during the reduction.

The electrochemical characterization and post-mortem SEM analysis of SOC with Ni/YSZ fuel electrode reduced at different temperatures provided in literature, for example, in the works of Jiao et al. [10] and Monzón et al. [39] demonstrate that higher reduction temperatures lead to the better SOC performance, better quality of Ni/YSZ interface and higher TPB length.

In this contribution, we present *in-situ* real-time observations of the initial reduction process of NiO/YSZ-compounds taken from fuel electrode supported SOCs performed with transmission electron microscopy under technically relevant operating conditions with hydrogen pressures varying from 13 kPa to 100 kPa in a temperature range of 200–850 °C. Microelectromechanical systems (MEMS)-based TEM holder allows us to broaden the pressure and temperature range of reduction conditions of NiO/YSZ. With three different reduction schemes, we demonstrate a strong dependence of Ni microstructure and Ni/YSZ interface quality on the reduction conditions. This also allows us to obtain a more complete picture of NiO/YSZ reduction at relevant conditions and re-evaluate previous *in-situ* TEM results obtained at lower temperatures and lower hydrogen pressures. In this work, the *in-situ* reduction of the NiO/YSZ fuel electrode is compared to pure NiO-samples to elucidate the influence of YSZ on the reduction process at moderate temperatures. The final microstructure of the fuel electrode reduced *in-situ* was compared with that of an *ex-situ* reduced fuel electrode to evaluate the impact of TEM sample preparation and the sample holder.

2. Experimental methodology

Using *in-situ* TEM atmosphere system from Protochips, we studied the electrode reduction at the H_2 pressures up to 1 atm and temperatures up to 850 °C which fit the real reduction condition of a solid oxide cell. Beforehand, electron transparent sample was prepared with a standard procedure [40–42] from a bulk fuel cell [15] with a focused ion beam (FIB) FEI Strata 400 S and placed on a MEMs-based chip for TEM analysis supplied by Protochips.

2.1. In-situ reduction schemes

In literature various reduction methodologies for NiO/YSZ fuel electrode material are described [12,43,44]. For example, the reduction can be carried out at moderate 500–600 °C or high temperatures of about 850 °C. Explorative reduction of NiO/YSZ has been tested even at lower temperatures of about 300–500 °C [45]. As mentioned above, the

reduction conditions such as temperature, time and gas type have a strong impact on the final microstructure of Ni/YSZ and cell performance. In this work, we investigate the influence of temperature on the microstructural changes in Ni/YSZ during the reduction in H_2 at relevel pressures with *in-situ* TEM. Due to the small sizes of TEM lamella, the time of reduction is much faster than in the bulk SOC and cannot be directly compared. Three reduction schemes were chosen – the first one starting from 200 °C with a gradual increase up to 850 °C, the second with the reduction performed straight at 850 °C and the third started at 850 °C, followed by the rapid temperature decrease to 400 °C and consequent increase back to 850 °C. To observe the reduction process at moderate temperatures in detail in the first scheme, we began with 27 kPa H_2 and 200 °C, then progressively increased to 100 kPa atm and 850 °C, as shown in Fig. 1. During the first reduction step the hydrogen pressure was maintained at constant 27 kPa, while the temperature was increased at a rate of 1 °C/s from 200 °C to 500 °C. During the second reduction step the pressure was increased to 40 kPa and temperature was raised from 500 °C to 650 °C by 1 °C/s and then kept constant for about 5 min. After no further significant rapid changes were observed in the sample, we proceeded with the final step at atmospheric pressure, increasing the temperature from 650 °C to 850 °C at the same speed. Then the sample was kept at 850 °C and 100 kPa H_2 for about 5 min to observe the transformation of Ni/YSZ microstructure at the operating temperatures of SOC, after Ni/YSZ was reduced at lower temperatures of 500–650 °C. After no significant morphological change had been detected, the first scheme was terminated. *In-situ* TEM observation was performed during the whole sequence. Grain orientation mapping and EELS maps were determined in between the reduction steps and at 200 °C, as marked with "analysis" in Fig. 1. Before the detailed analysis, the hydrogen gas was evacuated from the sample holder and sample was cooled down to 200 °C with a maximum rate of 5 °C/s to diminish possible microstructure changes related to further reduction or thermal stresses. After the analysis the temperature was increased with the same maximum rate to perform reduction steps 2 and 3.

Second reduction scheme closely replicates the actual reduction conditions of the bulk fuel electrode of SOC. The temperature was first increased to 850 °C and then the hydrogen was introduced to the sample holder with pressure of 40 kPa. The sample was held at these conditions for about 5 min.

Third reduction scheme serves purely explorative purpose to confirm the influence of temperature on the kinetics of NiO/YSZ reduction described later in the text. During the third reduction scheme, NiO reduction also started at 850 °C. Considering very rapid reduction kinetics of thin NiO/YSZ lamella at 850 °C (see Supplementary information), the temperature was decreased to 400 °C with a step of 5 °C/s just 3 s after the hydrogen gas introduction to the preheated sample. The temperature was increased again to 850 °C with the same step at 40 kPa H_2 pressure. After the temperature increase, the sample was kept at 850 °C and 40 kPa for about 3 min. The grain orientation mapping was performed before and after the complete reduction in the second and third case due to the rapid NiO reduction kinetics at high temperatures.

Pure NiO sample was reduced *in-situ* using the same reduction conditions as in the first case of NiO/YSZ reduction. Due to the absence of the supporting structure of YSZ, pure NiO sample remained mechanically stable only below 650 °C.

2.2. Grain orientation mapping

Initially, and after every reduction step the grain orientation of NiO/Ni and YSZ was determined with nanobeam electron diffraction using the NanoMEGAS ASTAR precession system installed at Thermo Fisher Scientific Themis 300 at 300 keV. The diffraction pattern was collected with a pixelated detector Dectris Quadro. To avoid any structural change in the sample throughout the acquisition of the grain orientation maps, the temperature was lowered to 200 °C (see Fig. 1) and hydrogen was evacuated from the atmosphere holder, followed by flushing with argon.

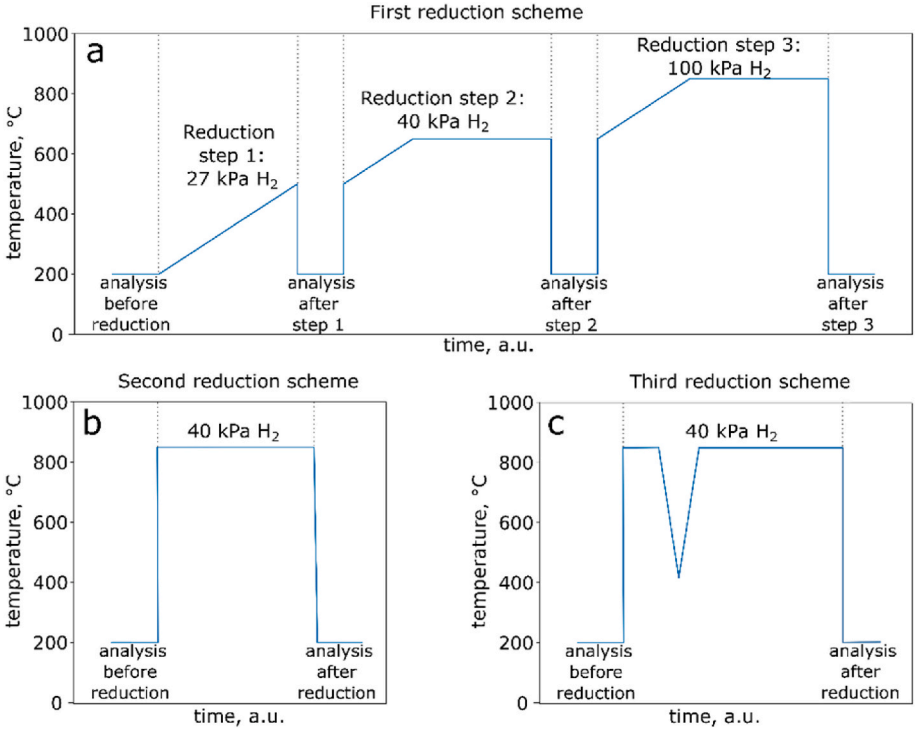

Fig. 1. Three reduction schemes of NiO/YSZ reduction with *in-situ* TEM. a. Reduction of NiO/YSZ is carried out in three steps: 1) from 200 °C to 500 °C at 27 kPa H_2; 2) at 650 °C and 40 kPa H_2; 3) at 850 °C and 100 kPa H_2. b. NiO/YSZ is reduced at 850 °C and 40 kPa H_2. c. Reduction of NiO/YSZ starts at 850 °C, followed by a rapid temperature drop with a step of 5 °C/s to 400 °C and consequent increase back to 850 °C. The H_2 pressure was kept at 40 kPa during the third reduction scheme. For each scheme the reduction and analysis were carried out during the same TEM session.

2.3. EELS measurements

EELS spectrometer and NanoMEGAS precession system are not available at the same microscope. Thus, to study the reduction of NiO, a different TEM lamella was prepared from the same fuel cell and reduced using the first reduction scheme described earlier. The reduction of Ni was assessed by the electron energy loss spectroscopy (EELS) at 300 keV at TFS Themis Z equipped with Gatan Continuum spectrometer and the spectra were acquired with Gatan K3 camera. The EELS maps were acquired initially and after every reduction step to determine the oxidation state of Ni. The reference L-edges of Ni oxide and metallic Ni were extracted from the EELS maps obtained before and after complete reduction, respectively, and then compared to the spectra found in literature [46]. The distribution of metallic Ni and NiO was measured with linear least squares (LLS) fitting of the experimental spectra using the provided references.

2.4. Ex-situ reduction

Complete *ex-situ* reduction of the bulk fuel cell samples is performed in test benches described in depth in Ref. [47]. Here, a pre-defined testing protocol with a stepwise increase of up to 100 % hydrogen is followed at high-temperatures of 800 °C. Partial *ex-situ* reduction of the same type of a fuel cell is carried out at a comparably lower temperature of 580 °C with only 27 % H_2 (balance N_2) at atmospheric pressure for 30 min. NiO/YSZ lamellas for *in-situ* TEM experiments with a thickness of 100–150 nm, reduce much faster than the bulk SOC. Therefore, the times of *ex-situ* and *in-situ* reductions cannot be identical. The reduction time of NiO/YSZ TEM samples was chosen empirically by observing the changes in the microstructure/composition during the *in-situ* TEM reduction. First *ex-situ* reduction scheme at 800 °C is a standard reduction procedure for this type of cells. Second *ex-situ* reduction scheme at 580 °C is chosen to confirm the validity of *in-situ* TEM reduction results at lower temperatures of 500–650 °C.

3. Results

3.1. Microstructural change of NiO/YSZ during first in-situ reduction scheme at moderate temperatures

Fig. 2 shows the grain orientation maps of NiO/YSZ (a) cermet and pure NiO (b) before reduction. High angle annular dark field (HAADF) STEM images, c,e,g,i, and annular dark images (ADF) STEM, d,f,h,k, on the same figure show the reduction progress and the microstructural evolution of NiO taken at different temperatures and 27 kPa H_2, for NiO/YSZ and pure NiO, respectively. Fig. 2a shows the polycrystalline grain structure of NiO/YSZ, with mean grain size of about 720 nm. The grain size of NiO, provided in Fig. 2b is much larger, so that just seven grains are visible in the chosen field of view. The grain orientation is shown in color code. No preferential grain orientation is observed, for both samples. At the very beginning of reduction, NiO grains appear slightly darker in the HAADF STEM image at Fig. 2c–e, whereas YSZ grains are brighter.

We observe the start of nickel oxide reduction in NiO/YSZ at 260 °C and 27 kPa H_2 (see the video 1). Fig. 2c shows the microstructure at slightly higher temperature of 271 °C where the reduction has already started in a few regions. These regions can be identified as 'cauliflower' areas with strong contrast variations in the HAADF STEM images. NiO starts to reduce from the triple junctions between NiO and YSZ, which are marked with yellow dots in Fig. 2c–e. Then the reduction front propagates along the phase boundaries and towards the middle of NiO grains, as visible in Fig. 2g at 288 °C. In a couple of cases, NiO reduction initiates from the centers of the grains, indicated by blue dots in Fig. 2c–e. A video of the initial reduction is available in the attachment, showing the findings even more clearly.

After the first reduction step, a porous microstructure is visible beside the Ni-grains in Fig. 2i. It forms due to oxygen loss and the related volume change. The presence of pores explains the cauliflower-like contrast appearance in the HAADF STEM images.

Supplementary data related to this article can be found online at https://doi.org/10.1016/j.jpowsour.2024.235626.

Multimedia component 2.

3.2. Microstructural change of pure NiO during in-situ reduction at moderate temperatures

At the same pressure of 27 kPa H_2, the reduction of the pure NiO starts at about 320 °C (see video 2) which is 50 °C higher than the start of the reduction of NiO/YSZ. The reduction initiates from the grain boundary triple junctions, marked with yellow dots on Fig. 2d, and from the grain boundaries, marked with light green lines on the same Figure. The images f,h,k show the reduction progress at higher temperatures (334 °C, 344 °C and 364 °C) during step 1 (see Fig. 1). Similar to the previous case of NiO/YSZ, the reduction front spreads along the grain boundaries and also extends towards the center of NiO grains, resulting in the formation of a porous structure.

Supplementary data related to this article can be found online at https://doi.org/10.1016/j.jpowsour.2024.235626.

Multimedia component 3.

3.3. Reduction of NiO measured with EELS

The EELS data presented in Fig. 3 was acquired after the NiO/YSZ sample was reduced under identical conditions as those used in the first step of the reduction scheme 1. EELS map with a corresponding HAADF STEM image given in Fig. 3, demonstrates the distribution of Ni and NiO in a NiO_x grain after exposure to 27 kPa H_2 and an increase in temperature to 500 °C. The Ni-containing grains exhibit many pores, visible as dark regions in Fig. 3a and b. The reference spectra of NiO and metallic Ni before and after complete reduction, are presented in Fig. 3c. The pores do not only propagate perpendicular to the surface of the lamella but also sideways forming channels which are clearly visible in Fig. 3a. NiO is detected at the edges of the channels and pores formed during the reduction. Ni grains are completely reduced after the sample was subjected to 40 kPa H_2 and a temperature of 650 °C during second reduction step (see Supplementary information).

3.4. Ni microstructure during first in-situ reduction scheme

According to the grain orientation map of the NiO/YSZ electrode before reduction in Fig. 2a, all the grain or phase boundaries have misorientations of more than 15°. Fig. 4 shows the grain orientation of Ni-containing grains before (a) and after each reduction step (b-d) included in the first reduction scheme. YSZ grains are removed from the crystal orientation maps for clarity. The corresponding HAADF-STEM images (e-h) are presented below each orientation map. The initial NiO grains in the polycrystal have an average diameter of about 800 nm. After the exposure to 27 kPa H_2 and the temperature increase to 500 °C (Fig. 4b) during the first step of reduction, Ni nanocrystals with an average diameter of about 100 nm develop. They form in the place of the initially large NiO grains. The Ni-nanocrystals are randomly oriented after the reduction. Thus, there is no preferred orientation relation between the initial NiO grains and the final Ni-nanograins.

Subsequent reduction at 40 kPa H_2 and 650 °C (Fig. 4c) leads to the increase of the average nanocrystal Ni grain size to 170 nm. This is attributed to Ni-grain growth and coarsening. The final reduction step at 850 °C and 100 kPa H_2 (Fig. 4d) causes further coarsening of the Ni grains, leading to an average domain size of about 340 nm.

During the second reduction step, we observe the volume decrease of the Ni grains with respect to the initial NiO grains by pore formation.

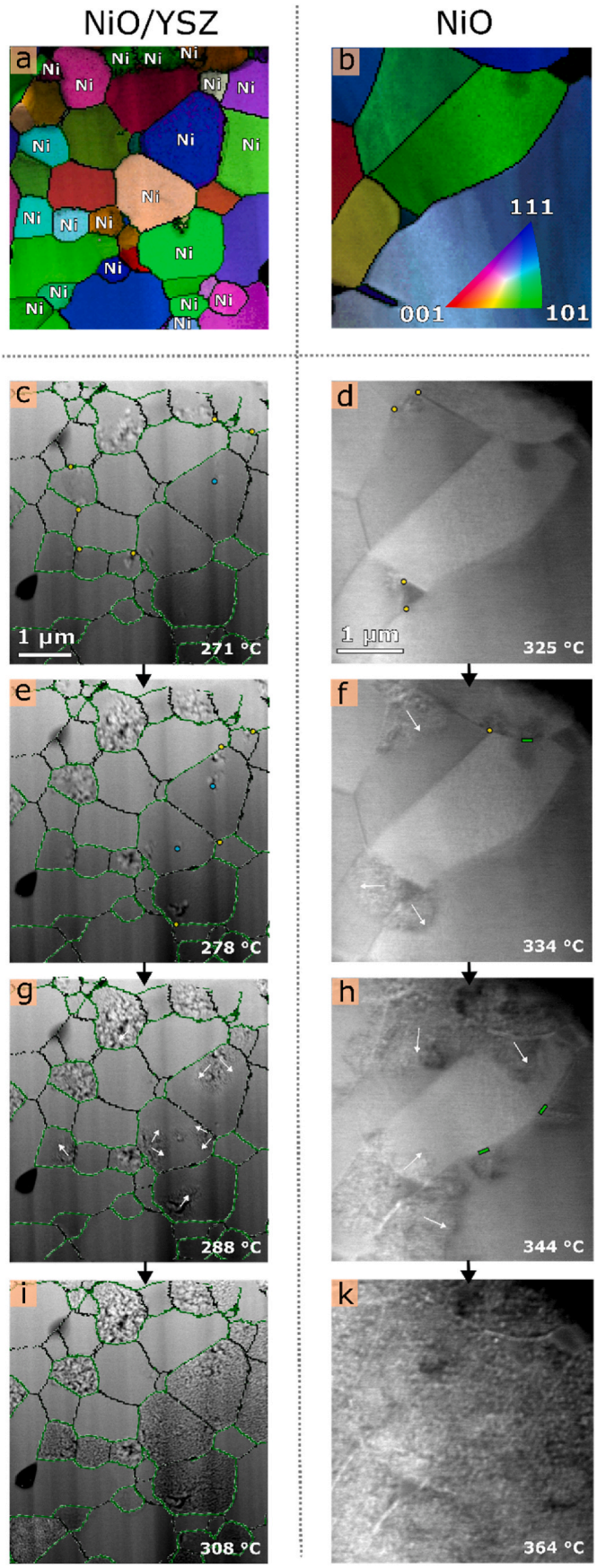

Fig. 2. Reduction of NiO/YSZ and pure Ni. *a. Grain orientation in NiO/YSZ cermet before the reduction in H_2. b. Grain orientation in pure NiO before the reduction in H_2. Both a and b are mapped with ASTAR precession electron diffraction. Dimensions of images a and b are the same as on c and d, correspondingly. c,e,g, i. HAADF STEM image series taken at different temperatures and 27 kPa H_2 pressure during in-situ reduction of NiO/YSZ. The phase boundaries between NiO_x and YSZ are marked with dark green and grain boundaries between NiO_x/NiO_x or YSZ/YSZ are marked with black lines. d, f, h, k. ADF STEM image series taken at different temperatures and 27 kPa H_2 pressure during in-situ reduction of pure NiO in the presence of 27 kPa H_2. Yellow dots indicate the start of NiO reduction at the triple junctions between NiO and YSZ grains, or NiO/NiO grains in case of pure Ni. Light green lines indicate the start of reduction at grain boundaries in case of pure NiO. Blue dots mark another starting point of NiO reduction: middle of NiO grain (possibly, crystalline defects or FIB artefact induced site). White arrows indicate the direction of the reduction front.*

(caption on next column)

Small pores formed during the initial reduction step, grow in size with the raise of temperature, as shown in the HAADF-STEM images in the second row of Fig. 4e–h.

At first, Ni-nanograin coarsening is accompanied by an increase of the number of larger pores while smaller ones vanish. After exposure to 100 kPa H_2 and 850 °C during the last reduction step, the pores inside Ni grains disappear (Fig. 4h). The gap between the initial phase boundaries of NiO and YSZ grow with the subsequent reduction steps, as visible in the HAADF images in the second row of Fig. 4, especially for the image taken after the last reduction step at 850 °C (Fig. 4h).

The slight tilt of TEM lamella, visible by the loss in sharpness in the HAADF STEM image in Fig. 4h, is caused by exposure to high temperatures and stresses arising during reduction. The vertical stripes visible in the HAADF-STEM images, result from the FIB curtaining artefact [48].

Like for the fuel cell electrode reduction, in the pure NiO sample individual grains become nanocrystalline and porous after the first reduction step with an average grain size of about 120 nm. With the absence of support structure of YSZ network, Ni grains lose connection between each other above 600 °C during the reduction step 2 at 40 kPa H_2. This leads to the fragmentation of the lamella. Grain orientation of NiO_x after reduction at 500 °C and 27 kPa H_2 is given in the Supplementary information.

3.5. Ni microstructure after the second and third in-situ reduction schemes

The microstructure of the sample before and after reduction is shown in Fig. 5a and b. The kinetics of the reduction is extremely fast at 850 °C and 40 kPa H_2. Just 5 s after hydrogen gas introduction to the preheated sample, the whole surface of NiO_x grains becomes porous. A slight increase in the pore size and minor grain shrinkage were observed after maintaining the sample under the same conditions for 5 min. A rapid change in the microstructure at the very beginning of the gas introduction, followed by only minor changes, suggests that the reduction mostly happens within first 5–20 s. The images demonstrating the intermediate changes in the NiO_x/YSZ microstructure are given in the Supplementary information. Fig. 5c and d demonstrates the grain orientations of NiO before reduction and Ni after reduction at 850 °C. Remarkably, each Ni grain remains single crystalline after the reduction. Large pores can be observed in the reduced Ni. Contradictory to the previous case, the pores do not disappear even after the exposure to high temperatures and high hydrogen pressures for 30 min (see Supplementary information).

The results of the third reduction scheme are demonstrated on Fig. 6. Intermediate drop in temperature to 400 °C from 850 °C led to the formation of the nanocrystalline Ni and almost complete absence of pores in the reduced Ni. Significant changes in the microstructure and volume of NiO_x grains during cooling and subsequent reheating indicate that the reduction was still ongoing (see Supplementary information). White lines in Fig. 6d demonstrate a high number of FCC twins which

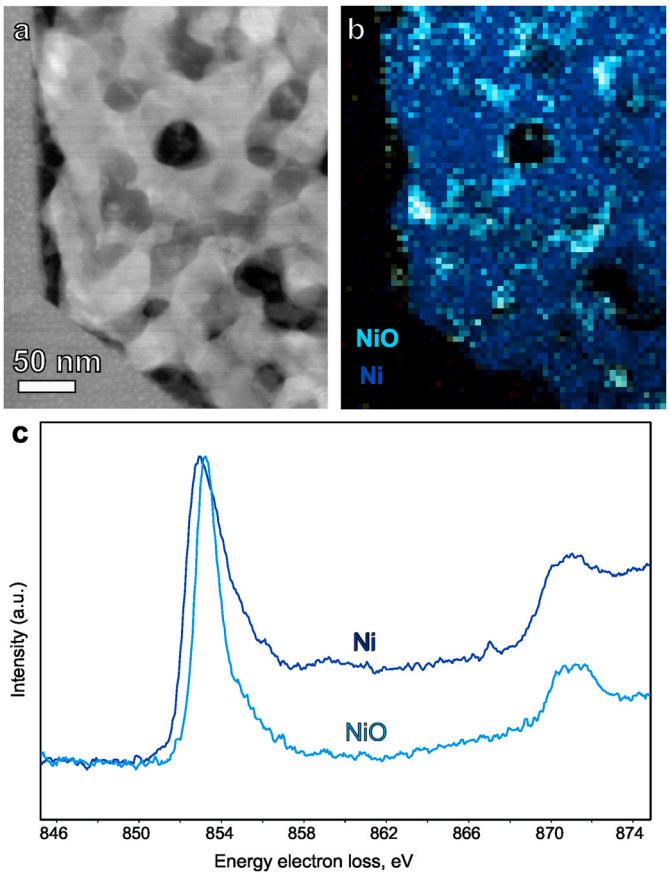

Fig. 3. EELS mapping of the partially reduced NiO_x grain. a. HAADF STEM image of Ni grain bordering YSZ after first reduction step with H_2 pressure of 27 kPa and temperature increase from 200 °C to 500 °C. b. EELS map of Ni oxidation state at the same area as in a. Oxidation state of Ni is determined with the reference fitting. c. Reference spectra of Ni L-edges are extracted from the same sample before reduction (NiO) and after complete reduction (metallic Ni) after step 3.

could be attributed to ∑3 {111} twin boundaries, appeared after the reduction.

The connection between Ni and YSZ is preserved better after the second and third reduction schemes than after the first.

3.6. *In-situ vs. ex-situ reduction*

The microstructures of the Ni/YSZ electrodes reduced *ex-situ* at 580 °C (Supplementary information) and *in-situ* at 500 °C (Figs. 3 and 4) are very similar: porous, nanocrystalline, not completely reduced and with a wide gap between Ni and YSZ.

After the *ex-situ* reduction at 800 °C Ni is completely reduced forming individual nanocrystalline Ni grains, which show brighter or darker gray diffraction contrast in ADF-STEM image in Fig. 8a while YSZ looks uniformly gray at the same image. Defects such as dislocations and small pores, are visible in the *ex-situ* and *in-situ* samples (Supplementary information). After the second *in-situ* reduction scheme, Ni preserved single crystalline orientation of the initial NiO grains and remained porous which differs from the *ex-situ* results.

After the first reduction scheme, the gap is present along all of the Ni/YSZ boundaries (Fig. 4h). After the second and third reduction scheme better connection can be observed between Ni and YSZ in Figs. 5b and 6b. In case of the *ex-situ*-reduction, the gap exists only along large pores which, probably, are formed in a place of the pre-existing pore network, where NiO came in contact with the H_2 during initial reduction (Fig. 8a). Otherwise, the interface between Ni and YSZ is crystalline as can be seen in Supplementary Information.

4. Discussion

4.1. *Reduction mechanism*

Due to the very small thickness of TEM lamellas below 100–150 nm, we assume that the reduction kinetics of NiO/YSZ during *in-situ* TEM experiment is mostly governed by nucleation [22] and can be described by JMAK model [25–27]. The kinetics of Ni reduction at different temperatures plays a major role in NiO/YSZ reduction mechanism. With three different reduction schemes we obtain contrasting final microstructures and morphologies of Ni. The reduction conditions also

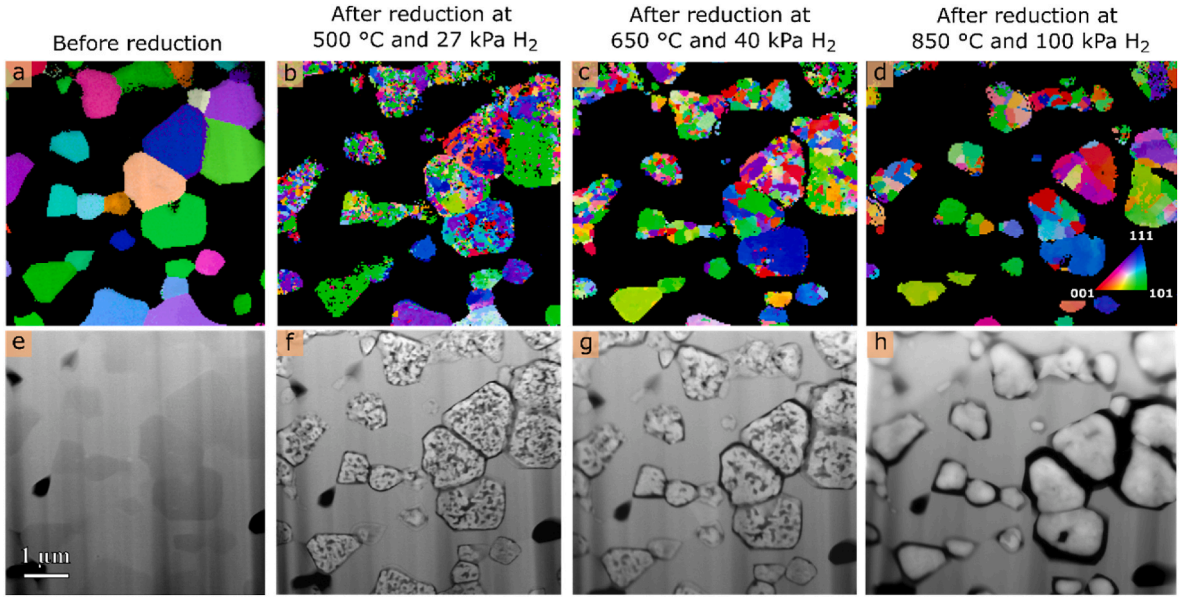

Fig. 4. Grain orientation mapping of Ni-containing grains (a–d) with corresponding HAADF STEM images (e–h) before and after three reduction steps for the first reduction scheme (see Fig. 1). Individual NiO grains become nanocrystalline after reduction. Large pores develop inside the initial NiO-grain regions and at the phase and grain boundaries.

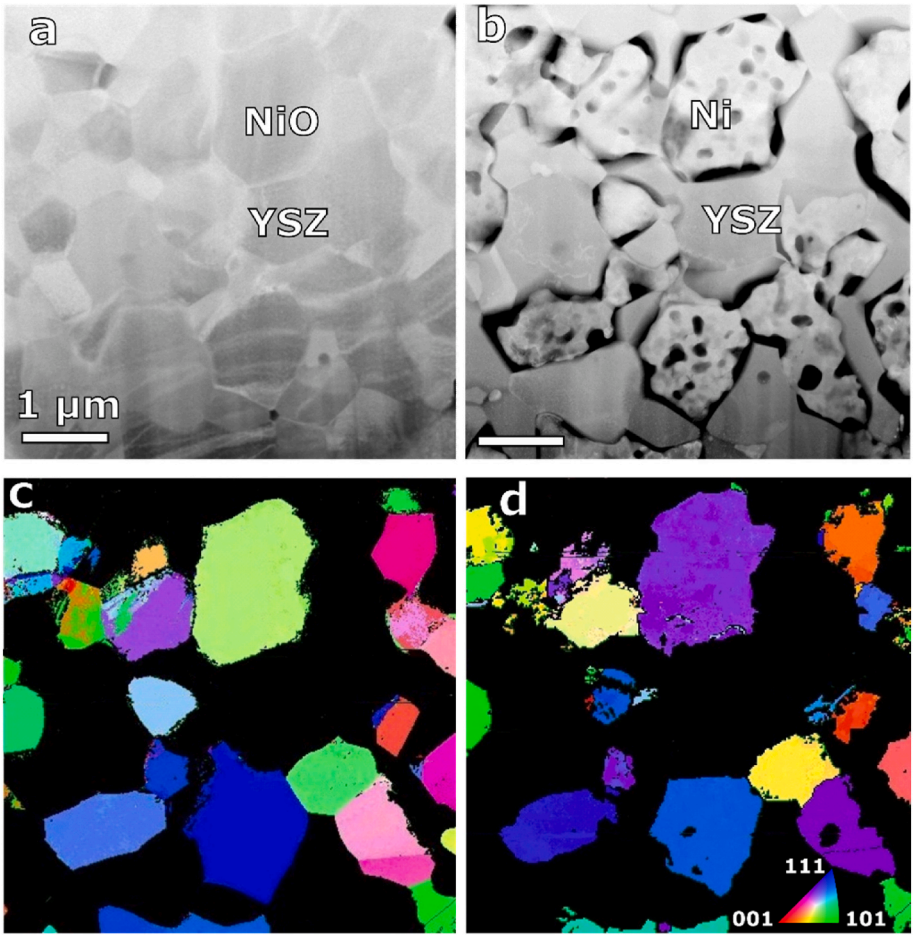

Fig. 5. ADF STEM images (a,b) before and after second reduction scheme with corresponding grain orientation mapping of Ni-containing grains (c,d). Ni grains preserved single crystallinity of NiO grains. Ni grains overlapping with YSZ are excluded from the grain orientation maps. The difference in orientation between NiO and Ni grains can be explained by the tilt of the TEM lamella which happened due to mechanical stresses during the exposure to high temperatures.

influence the quality of the interface between Ni and YSZ or connectivity of Ni grains. Within the chosen range of hydrogen pressures from 27 kPa to 101 kPa, temperature plays a major role in the reduction kinetics. As mentioned in the introduction, formation of the Ni nuclei is strongly affected by the temperature. With the temperature rise, the amount of initial Ni nuclei increases and nucleation can start not only at the phase/grain boundaries but also at the whole surface of the grains [28]. A sketch of the mechanisms taking place at different temperatures, is presented in Fig. 7.

For the first reduction scheme, the formation of nanocrystalline Ni in place of the initial NiO grains hints at multiple but sparse nucleation points. First nuclei are formed at triple junctions between NiO and YSZ grains and phase/grain boundaries (see Fig. 2). NiO reduction at the nucleus sites leads to the local lattice shrinkage and elastic stress. Stress release is associated with the formation of pores [49] visible in Figs. 2 and 3 and dislocations (see Supplementary Information). Further NiO-reduction at the hydrogen gas and NiO interface leads to pore extension and pore channel formation. Interface between reduced Ni and NiO has a higher amount of oxygen or nickel vacancies due to the lattice mismatch. It has been shown that the oxygen can be transferred from NiO to Ni easier in the presence of oxygen vacancy [50,51] and Ni can diffuse into NiO in the presence of Ni vacancy [51]. Therefore, the pore formation could also be promoted by the diffusion of vacancies at the reduction front between NiO and Ni. The reaction front propagates from the initial nucleation sites at triple junctions between NiO/YSZ grains and phase/grain boundaries towards the inside of the grains confirming the autocatalytic nature of this reaction. Initial nickel clusters rotate with respect to the NiO lattice forming nanocrystalline microstructure of the reduced Ni.

In a few instances, the reduction started in the middle of the NiO grain in the NiO/YSZ electrode (Fig. 2b). This could be an effect related to the TEM lamella: the location is found in vicinity to the FIB curtaining artefact which might have created sharp edges in the middle of NiO grain. Angelis et al. [52] suggested that during reduction NiO/YSZ the system tends to minimize the surface energy of reducing Ni by eliminating sharp edges and minimizing surface curvatures. Therefore, the initiation of reduction at the sharp edges created by FIB preparation, may also be linked to the surface energy minimization process. The presence of crystallographic defects inside NiO grain such as oxygen vacancies, offers an alternative explanation. As mentioned above, NiO reduction process observed in this work is similar in NiO/YSZ and pure NiO in the range of 200–500 °C. We observe the start of the reduction at the triple junctions followed by phase boundaries (when YSZ is present) and then grain boundaries (see video in the attachment). Higher energy regions might promote local energy reduction by the formation of a new phase, in this case the Ni-phase. Experimental studies in metallic copper [53] confirm that triple junctions can have higher energy than grain boundaries. The energies of the phase boundaries in ceramics can also have higher energies that grain boundaries [54]. Higher amount of defects at triple junctions and phase/grain boundaries [55], in particular oxygen vacancies in NiO, can also promote the start of the reduction in these regions [50,56].

The reduction of pure NiO started at higher temperature of 320 °C compared to 260 °C for NiO in YSZ. The onset of reduction at earlier

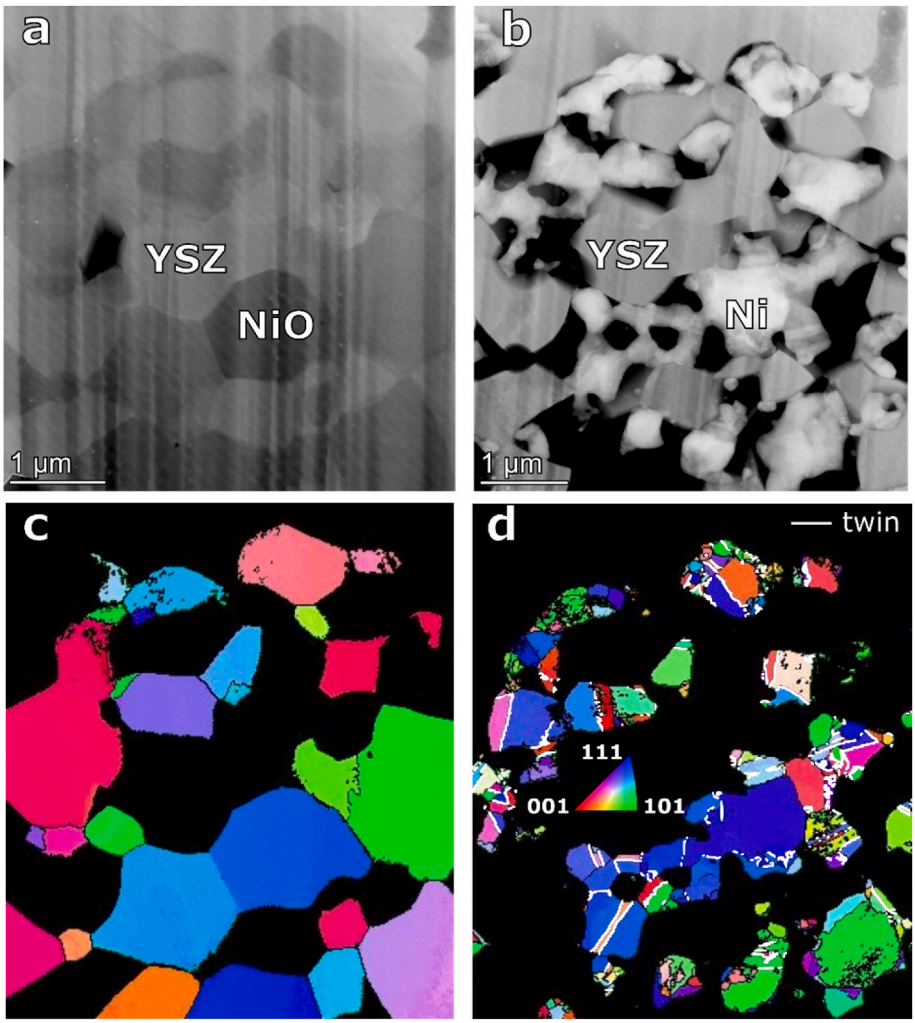

Fig. 6. ADF STEM images (a,b) before and after third reduction scheme with corresponding grain orientation mapping of Ni-containing grains (c,d). Ni grains became nanocrystalline after the lowering the temperature to 400 °C from 850 °C in the middle of the reduction.

temperatures in the fuel electrode suggests higher excess energies of the triple junctions between NiO and YSZ than pure NiO/NiO triple junctions leading to formation of Ni nuclei at lower temperatures. Transfer of oxygen ions to the ion conductor YSZ was proposed by Jeangros et al. [32] as one of the contributors to NiO reduction in the YSZ matrix. This could be another factor contributing to the onset of the reduction at lower temperatures in NiO/YSZ compared to pure NiO.

The reduction of NiO/YSZ at 850 °C during second reduction scheme resulted in the preservation of the single crystallinity in almost every reduced Ni grain. This suggests that a homogeneous reduction front with closely spaced Ni nuclei propagates through the initial NiO grains without breaking the single crystallinity as shown in Fig. 7. Interestingly enough, initial grain boundaries in NiO in most cases remain in the same place in the reduced Ni, possibly serving as a barrier for the propagation of the reduction front. Differently from the first reduction scheme, Ni grains are still porous after the reduction at 850 °C suggesting that the single crystallinity of each grain prevented them from coarsening. Notably, the creation of pores does not lead to the rotation or interruption of the reduction front, at least at high temperatures.

As can be seen in Fig. 5, after the reduction many of the Ni grains, even with high angle grain boundaries remained connected to each other. Contradictory to that, after the reduction at low temperatures the connection between Ni grains is destroyed (Figs. 4 and 7). Good connection between two Ni grains in Ni/YSZ fuel electrode was observed in the literature [32] only for low angle coherent grain boundaries in Ni/YSZ after reduction at low temperatures and low hydrogen pressures.

The reduction of temperature from 850 °C to 400 °C during the third reduction scheme led to the formation of the nanocrystalline microstructure in the reduced Ni grains. Possible mechanism could be described as follows: the number of newly formed Ni nuclei decreases with the temperature reduction leading to the interruption of the homogeneous reduction front and rotation of newly forming Ni clusters with respect to the NiO lattice. This support the hypnosis of Manukyan [28] that the Ni nuclei should be closely spaced for the preservation of single crystallinity. After ramping the temperature back up to 850 °C, the final Ni microstructure contains a large number of FCC twin boundaries, possibly $\sum 3$ {111} type marked with white lines in Fig. 6. Presence of the twin boundaries can modify mechanical [57] and electrical [58] properties of Ni. Hydrogen is known to reduce the energy formation of stacking faults and promote mechanical twinning in steels [59,60]. However, formation of twins was not observed during the first scheme when the sample with nanocrystalline Ni was cooled down for analysis and then subsequently re-heated with the same heating rate in between steps 1 and 2 or 2 and 3. In case of the third reduction scheme, twin formation induced by hydrogen may also arise from higher mechanical stresses compared to the first reduction scheme. These stresses could appear due to the interruption of the homogeneous reduction front between the already reduced epitaxial single-crystalline Ni layer and the remaining NiO_x during sample cooling to 400 °C and subsequent reheating (see Fig. 7).

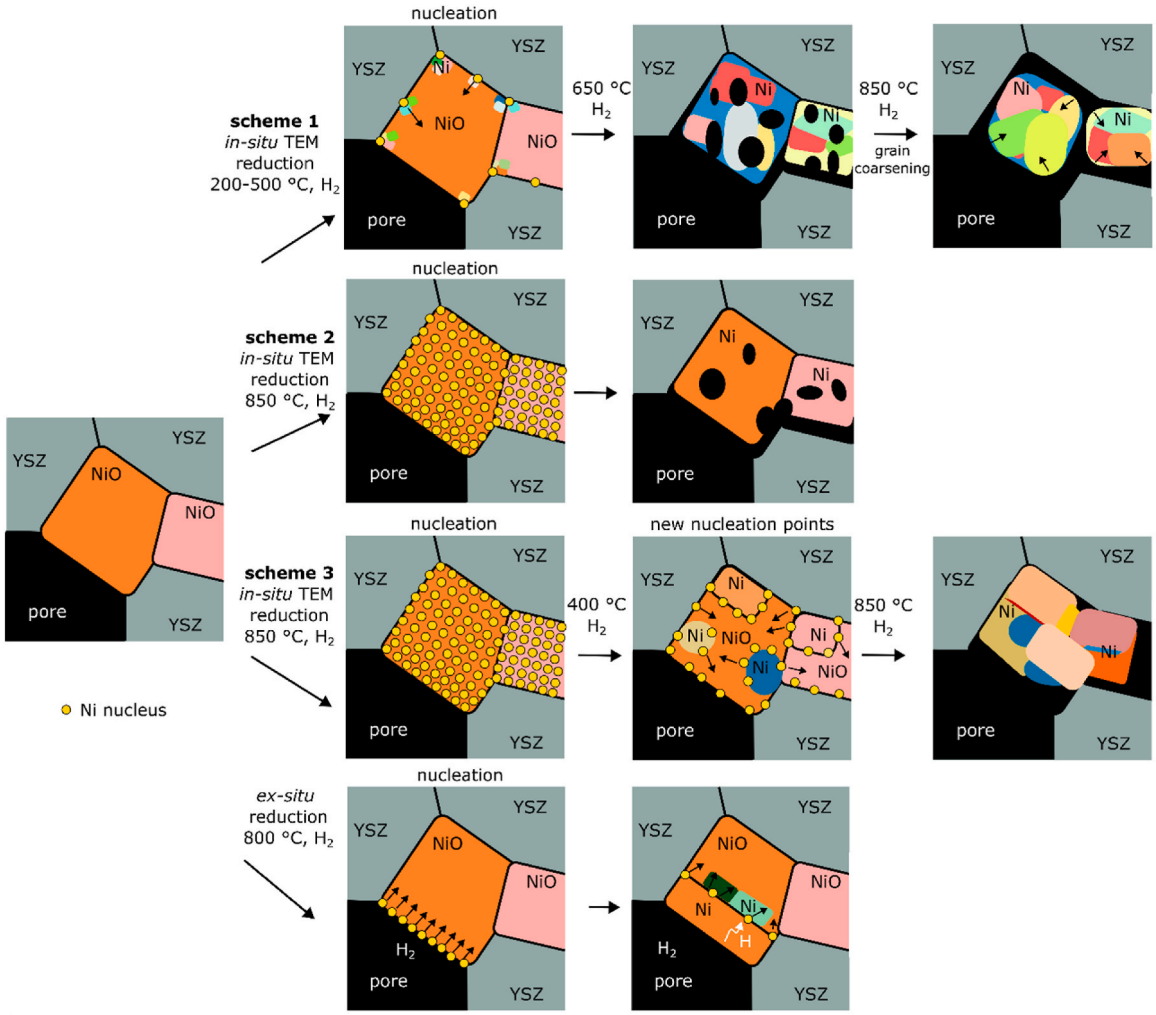

Fig. 7. A sketch of the NiO/YSZ reduction mechanisms taking place during three reduction schemes carried out with the *in-situ* TEM, compared to the *ex-situ* reduction of the bulk NiO/YSZ mechanism at high temperatures.

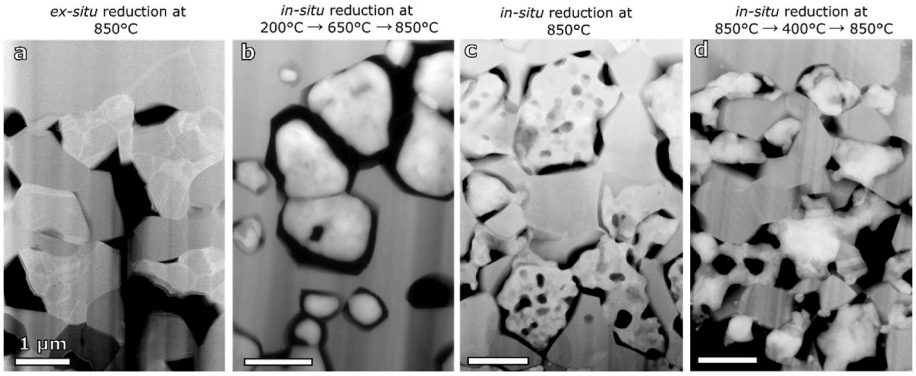

Fig. 8. Microstructure of Ni-YSZ after reduction *ex-situ* and *in-situ*. a. ADF-STEM image of Ni/YSZ electrode of a SOC reduced *ex-situ* at 800 °C. b. ADF-STEM image of Ni/YSZ electrode reduced *in-situ* using a first reduction scheme, with a gradual increase of temperature: 200 °C → 650 °C → 850 °C. c. ADF-STEM image of Ni/YSZ electrode reduced *in-situ* with a second reduction scheme at 850 °C. d. ADF-STEM image of Ni/YSZ electrode reduced *in-situ* with a third reduction scheme starting at 850 °C, decreasing the temperature to 400 °C with a consequent increase back to 850 °C.

After the third reduction scheme Ni does not contain pores. The disappearance of the pores is linked to the exposure of nanocrystalline Ni to high temperatures as shown in the first and confirmed with the third reduction schemes. In the second case, single crystalline Ni grains remain porous, at least in the time frame of the experiment. Therefore, nanocrystallinity of Ni can be one of the main factors in Ni grain coarsening.

4.2. *Influence of the in-situ TEM conditions on the reaction process*

Small sizes of the TEM lamella and sample interaction with the electron beam can alter the processes observed with *in-situ* TEM from the

bulk case. For example, after reduction in TEM at 850 °C individual Ni grains remained single crystalline and porous. On the other hand, after *ex-situ* reduction, Ni became nanocrystalline without the presence of the large pores. In this case, the size of the sample clearly plays a major role. In the bulk NiO/YSZ material for fuel electrode NiO grains are about 1–2 μm in size. The reduction of NiO in this material can be approximated with a shrinking core model [61] where the diffusion of hydrogen through already reduced Ni to the core of the grain starts to be a limiting factor for the reaction speed as illustrated in Fig. 7. On the other hand, the thickness of a standard TEM lamella is below 100–150 nm. According to Richardson et al. [22], the shape and size of nanoparticles with diameters of 7–163 nm do not impact the reaction speed. The total surface of NiO grains initially exposed to hydrogen can also contribute to the reduction kinetic. In case of the TEM experiment, the whole surface of the sample is exposed to hydrogen creating more nucleation points at the surface of the grain at high temperatures.

In the bulk cell, hydrogen is supplied to NiO trough the 3D network of pores, limiting the contact areas. Extrapolating the TEM reduction results to bulk SOC, at low reduction temperatures (200–500 °C), the NiO/YSZ reduction would initiate primarily at triple junctions and phase boundaries that are exposed to hydrogen through the 3D pore network. In contrast, at higher temperatures (around 850 °C), the reduction would begin across the entire surface of the NiO grains in contact with hydrogen.

Electron beam could create oxygen vacancies in NiO [62] which facilitate the dissociation of hydrogen molecules at the surface of NiO. In the previous studies, the influence of the electron beam on NiO reduction was found insignificant [36]. However, preservation of the single crystallinity of each individual NiO grain was observed in the literature only above 900 °C at similar hydrogen pressures. Single crystallinity of Ni grains detected in this work after reduction at lower temperatures of 850 °C can be explained firstly, by the small sizes of the TEM lamella and, secondly, by the higher amount of oxygen vacancies accelerating the reduction process.

4.3. *Influence of the reduction process on triple phase boundaries*

The microstructure of the Ni/YSZ electrode reduced *ex-situ* at different temperatures suggests that the initial reduction temperature is very important with respect to the length, density and good crystalline connection between solid phases of the TPBs - Ni/YSZ/gas phase - in the solid oxide cell. Reduction at 580 °C leads to a wide gap between Ni and YSZ, making TPBs almost non-existent. This would lead to a comparably insufficient electrochemical performance of the cell. This gap is definitely created by the start of the reduction at the grain boundaries. According to *in-situ* experiment, further increase of temperature during reduction induces the coarsening of the Ni grains but does not seal the gap between Ni and YSZ (see Figs. 4 and 7). On the other hand, TPBs created in the sample reduced *ex-situ* at 800 °C, are of comparably good quality. *In-situ* results confirm that high initial reduction temperatures are preferred for better Ni-YSZ interface quality. Moreover, the quick drop of temperature during the reduction does not affect final Ni-YSZ interface quality but modifies the microstructure of the reduced Ni. This intentional modification could be adopted in bulk SOCs with the adjustments of temperature and time of the reduction.

In conclusion, faster reduction kinetics and initiation of the reduction at the whole interface between NiO and gas contribute to the higher TPBs length and density together with better crystalline connection between solid phases. The quality of TPB is known as one of the major factors in the SOC performance and degradation mechanism [63]. Therefore, the higher initial reduction temperatures should be preferred.

5. Conclusions

With *in-situ* gas TEM performed at real conditions, we observe the NiO reduction in a NiO/YSZ fuel cell electrode at different temperatures in real time. We show the importance of closely replicating the exact conditions of bulk NiO/YSZ reduction with *in-situ* TEM by demonstrating the detrimental effect of temperature on the final Ni microstructure with three reduction schemes at relevant hydrogen pressures. Broadening the range of temperature and pressure allows us to obtain a clearer and more relevant picture of Ni/YSZ reduction at the nanoscale re-evaluating previous results obtained in ETEM.

For the first time, we demonstrate that initial high reduction temperatures at relevant hydrogen pressures of about 40 kPa H_2 lead to the preservation of single crystallinity in each Ni grain, better connection between Ni grains and superior quality of Ni/YSZ interface.

At high temperatures, nanocrystallinity of the reduced Ni can be one of the main forces in the grain coarsening causing the grain shrinkage and the disappearance of pores.

By comparing direct *in-situ* observations and *ex-situ* analysis, we demonstrate that the starting reduction temperature has a detrimental effect on the final length of the triple phase boundaries and the connection between Ni and YSZ. In the temperature range between 200 and 500 °C the *in-situ* reduction starts from the NiO/YSZ triple junctions, then from phase boundaries followed by the grain boundaries creating a wide gap between Ni and YSZ, also observed in the literature on NiO/YSZ reduction in ETEM. Novel *in-situ* TEM results from this work show that the reduction of NiO/YSZ at high temperatures of 800–850 °C and relevant for SOC hydrogen pressures starts from the whole interface between NiO and gas leading to the better Ni-YSZ connection. Real-time *in-situ* TEM observations provide deeper insights into NiO/YSZ reduction, confirming the literature evidence that higher reduction temperatures result in an improved Ni/YSZ interface. Initial superior triple phase boundary quality obtained at higher temperatures can potentially enhance the performance of the electrode.

6. Future prospects

The outcome of this work could be applied to the production of various types of fuel electrodes that require NiO reduction. In addition to the general conclusion that higher reduction temperatures result in an improved interface between Ni and the solid electrolyte, the Ni microstructure could also be tailored. For example, to replicate the single crystallinity of each Ni grain in the bulk cell, higher temperatures may be required or/and larger contact areas between NiO and gas. However, the *in-situ* reduction conditions from this work could be directly replicated to achieve a desired microstructure for the production of Ni nanoelectrodes due to their small size, similar to the TEM lamella. The intermediate short reduction of temperature could be used to produce twins in Ni preserving the quality of Ni/YSZ interface.

CRediT authorship contribution statement

S. Korneychuk: Writing – review & editing, Writing – original draft, Visualization, Validation, Methodology, Investigation, Formal analysis, Data curation, Conceptualization. **C. Grosselindemann:** Writing – review & editing, Methodology, Investigation. **N.H. Menzler:** Writing – review & editing, Supervision, Resources, Methodology, Funding acquisition. **A. Weber:** Writing – review & editing, Validation, Supervision, Resources, Project administration, Methodology, Funding acquisition. **A. Pundt:** Writing – review & editing, Supervision, Project administration, Funding acquisition, Conceptualization.

Declaration of competing interest

The authors declare that they have no known competing financial interests or personal relationships that could have appeared to influence the work reported in this paper.

Acknowledgements

The Helmholtz Association of German Research Centers (HGF) and the Federal Ministry of Education and Research (BMBF), Germany are gratefully acknowledged for supporting the development of solar powered technologies for H2 generation within the frame of the Innovation Pool project "Solar H2: Highly Pure and Compressed" and the Helmholtz Research Program "Materials and Technologies for the Energy Transition" (MTET). *This work was partly carried out with the support of the Karlsruhe Nano Micro Facility (KNMFi, www.knmf.kit.edu), a Helmholtz Research Infrastructure at Karlsruhe Institute of Technology (KIT, www.kit.edu). This work was partly carried out with the support of the Joint Laboratory Model and Data-driven Materials Characterization (JL MDMC), a cross-center platform of the Helmholtz Association.*

Appendix A. Supplementary data

Supplementary data to this article can be found online at https://doi.org/10.1016/j.jpowsour.2024.235626.

Data availability

Data will be made available on request.

References

[1] G. Rinaldi, A. Nakajo, P. Burdet, M. Cantoni, W.K.S. Chiu, J. Van herle, Characterization of local morphology and availability of triple-phase boundaries in solid oxide cell electrodes, Acta Mater. 178 (2019) 194–206, https://doi.org/10.1016/J.ACTAMAT.2019.07.027.

[2] H. Apfel, M. Rzepka, H. Tu, U. Stimming, Thermal start-up behaviour and thermal management of SOFC's, J. Power Sources 154 (2) (2006) 370–378, https://doi.org/10.1016/J.JPOWSOUR.2005.10.052.

[3] P. Holtappels, H. Mehling, S. Roehlich, S.S. Liebermann, U. Stimming, SOFC system operating strategies for mobile applications, Fuel Cell. 5 (4) (2005) 499–508, https://doi.org/10.1002/FUCE.200400088.

[4] W. Schafbauer, N.H. Menzler, H.P. Buchkremer, Tape casting of anode supports for solid oxide fuel cells at forschungszentrum Jülich, Int. J. Appl. Ceram. Technol. 11 (1) (2014) 125–135, https://doi.org/10.1111/J.1744-7402.2012.02839.X.

[5] R.I. Tomov, M. Krauz, A. Tluczek, et al., Vacuum-sintered stainless steel porous supports for inkjet printing of functional SOFC coatings, Mater. Renew Sustain. Energy 4 (3) (2015) 1–11, https://doi.org/10.1007/S40243-015-0056-7.

[6] N.H. Menzler, J. Malzbender, P. Schoderböck, R. Kauert, H.P. Buchkremer, Sequential tape casting of anode-supported solid oxide fuel cells, Fuel Cell. 14 (1) (2014) 96–106, https://doi.org/10.1002/FUCE.201300153.

[7] T. Klemensø, C.C. Appel, M. Mogensen, In situ observations of microstructural changes in SOFC anodes during redox cycling, Electrochem. Solid State Lett. 9 (9) (2006) A403, https://doi.org/10.1149/1.2214303.

[8] M. Pihlatie, A. Kaiser, P.H. Larsen, M. Mogensen, Dimensional behavior of Ni–YSZ composites during redox cycling, J. Electrochem. Soc. 156 (3) (2009) B322, https://doi.org/10.1149/1.3046121.

[9] H. Monzón, M.A. Laguna-Bercero, The influence of the reducing conditions on the final microstructure and performance of nickel-yttria stabilized zirconia cermets, Electrochim. Acta 221 (2016) 41–47, https://doi.org/10.1016/J.ELECTACTA.2016.10.152.

[10] Z. Jiao, N. Shikazono, Quantitative study on the correlation between solid oxide fuel cell Ni-YSZ composite anode performance and reduction temperature based on three-dimensional reconstruction, J. Electrochem. Soc. 162 (6) (2015) F571–F578, https://doi.org/10.1149/2.0721506JES.

[11] M.H. Pihlatie, A. Kaiser, M. Mogensen, M. Chen, Electrical conductivity of Ni–YSZ composites: degradation due to Ni particle growth, Solid State Ionics 189 (1) (2011) 82–90, https://doi.org/10.1016/J.SSI.2011.02.001.

[12] S. Vafaeenezhad, A.R. Hanifi, M.A. Laguna-Bercero, T.H. Etsell, P. Sarkar, Microstructure and long-Term stability of Ni-YSZ anode supported fuel cells: a review, Mater. Futures 1 (4) (2022), https://doi.org/10.1088/2752-5724/AC88E7.

[13] A. Leonide, V. Sonn, A. Weber, E. Ivers-Tiffée, Evaluation and modeling of the cell resistance in anode-supported solid oxide fuel cells, J. Electrochem. Soc. 155 (1) (2008) B36, https://doi.org/10.1149/1.2801372.

[14] S. Dierickx, T. Mundloch, A. Weber, E. Ivers-Tiffée, Advanced impedance model for double-layered solid oxide fuel cell cermet anodes, J. Power Sources 415 (2019) 69–82, https://doi.org/10.1016/J.JPOWSOUR.2019.01.043.

[15] D. Udomsilp, C. Lenser, O. Guillon, N.H. Menzler, Performance benchmark of planar solid oxide cells based on material development and designs, Energy Technol. 9 (4) (2021) 2001062, https://doi.org/10.1002/ENTE.202001062.

[16] J. Joos, M. Ender, I. Rotscholl, N.H. Menzler, E. Ivers-Tiffée, Quantification of double-layer Ni/YSZ fuel cell anodes from focused ion beam tomography data, J. Power Sources 246 (2014) 819–830, https://doi.org/10.1016/J.JPOWSOUR.2013.08.021.

[17] Y.H. Lee, H. Muroyama, T. Matsui, K. Eguchi, Degradation of nickel-yttria-stabilized zirconia anode in solid oxide fuel cells under changing temperature and humidity conditions, J. Power Sources 262 (2014) 451–456, https://doi.org/10.1016/J.JPOWSOUR.2014.03.031.

[18] S.W. Cheng, C.H. Tsai, S.H. Wu, C.K. Liu, Y.N. Cheng, R.Y. Lee, Effects of reduction process on the electrochemical and microstructural properties for electrolyte-supported SOFC, Int. J. Hydrogen Energy 40 (3) (2015) 1534–1540, https://doi.org/10.1016/J.IJHYDENE.2014.11.034.

[19] M. Lang, S. Raab, M.S. Lemcke, C. Bohn, M. Pysik, Long-Term behavior of a solid oxide electrolyzer (SOEC) stack, Fuel Cell. 20 (6) (2020) 690–700, https://doi.org/10.1002/FUCE.201900245.

[20] Q. Fang, N.H. Menzler, Long-term stack tests, in: High-Temperature Electrolysis: from Fundamentals to Applications, IOP Publishing, 2023, https://doi.org/10.1088/978-0-7503-3951-3ch10.

[21] J. Schefold, H. Poepke, A. Brisse, Solid oxide electrolyser cell testing up to the above 30,000 h time range, ECS Trans. 97 (7) (2020) 553–563, https://doi.org/10.1149/09707.0553ECST.

[22] J.T. Richardson, R. Scates, M.V. Twigg, X-ray diffraction study of nickel oxide reduction by hydrogen, Appl. Catal. Gen. 246 (1) (2003) 137–150, https://doi.org/10.1016/S0926-860X(02)00669-5.

[23] A.F. Benton, P.H. Emmett, The reduction of nickelous and ferric oxides by hydrogen, J. Am. Chem. Soc. 46 (12) (1924) 2728–2737, https://doi.org/10.1021/JA01677A018/ASSET/JA01677A018.

[24] G.B. Taylor, H.W. Starkweather, Reduction of metal oxides by hydrogen, J. Am. Chem. Soc. 52 (6) (1930) 2314–2325, https://doi.org/10.1021/JA01369A019/ASSET/JA01369A019.

[25] M. Avrami, Granulation, phase change, and microstructure kinetics of phase change. III, J. Chem. Phys. 9 (2) (1941) 177–184, https://doi.org/10.1063/1.1750872.

[26] M. Avrami, Kinetics of phase change. II Transformation-time relations for random distribution of nuclei, J. Chem. Phys. 8 (2) (1940) 212–224, https://doi.org/10.1063/1.1750631.

[27] M. Avrami, Kinetics of phase change. I general theory, J. Chem. Phys. 7 (12) (1939) 1103–1112, https://doi.org/10.1063/1.1750380.

[28] K.V. Manukyan, A.G. Avetisyan, C.E. Shuck, et al., Nickel oxide reduction by hydrogen: kinetics and structural transformations, J. Phys. Chem. C 119 (28) (2015) 16131–16138, https://doi.org/10.1021/ACS.JPCC.5B04313.

[29] D.S. Lee, M. Dongjoon, A kinetics of hydrogen reduction of nickel oxide at moderate temperature, Met. Mater. Int. 25 (4) (2019) 982–990, https://doi.org/10.1007/S12540-019-00261-Y.

[30] J. Bandrowski, C.R. Bickling, K.H. Yang, O.A. Hougen, Kinetics of the reduction of nickel oxide by hydrogen, Chem. Eng. Sci. 17 (5) (1962) 379–390, https://doi.org/10.1016/0009-2509(62)80039-6.

[31] S. Ogawa, R. Taga, A. Yoshigoe, Y. Takakuwa, Two-step model for reduction reaction of ultrathin nickel oxide by hydrogen, J. Vac. Sci. Technol. A: Vacuum, Surfaces, and Films 39 (4) (2021), https://doi.org/10.1116/6.0001056/247280.

[32] Q. Jeangros, A. Faes, J.B. Wagner, et al., In situ redox cycle of a nickel–YSZ fuel cell anode in an environmental transmission electron microscope, Acta Mater. 58 (14) (2010) 4578–4589, https://doi.org/10.1016/J.ACTAMAT.2010.04.019.

[33] D. Klotz, B. Butz, A. Leonide, J. Hayd, D. Gerthsen, E. Ivers-Tiffée, Performance enhancement of SOFC anode through electrochemically induced Ni/YSZ nanostructures, J. Electrochem. Soc. 158 (6) (2011) B587–B595, https://doi.org/10.1149/1.3569727.

[34] D. Waldbillig, A. Wood, D.G. Ivey, Electrochemical and microstructural characterization of the redox tolerance of solid oxide fuel cell anodes, J. Power Sources 145 (2) (2005) 206–215, https://doi.org/10.1016/J.JPOWSOUR.2004.12.071.

[35] S.B. Simonsen, K. Agersted, K.V. Hansen, et al., Environmental TEM study of the dynamic nanoscaled morphology of NiO/YSZ during reduction, Appl. Catal. Gen. 489 (2015) 147–154, https://doi.org/10.1016/J.APCATA.2014.10.045.

[36] S.B. Simonsen, K. Agersted, K.V. Hansen, et al., NiO/YSZ reduction for SOFC/SOEC studied in situ by environmental transmission electron microscopy, ECS Trans. 64 (2) (2014) 73–80, https://doi.org/10.1149/06402.0073ECST.

[37] A. Faes, Q. Jeangros, J.B. Wagner, et al., In situ reduction and oxidation of nickel from solid oxide fuel cells in a, Trans. Elect. Micro. E C S Transact. 25 (2) (2009) 1985–1992, https://doi.org/10.1149/1.3205743.

[38] Q. Jeangros, A.B. Aebersold, C. Hébert, J. Van herle, A. Hessler-Wyser, A TEM study of Ni interfaces formed during activation of SOFC anodes in H2: influence of grain boundary symmetry and segregation of impurities, Acta Mater. 103 (2016) 442–447, https://doi.org/10.1016/J.ACTAMAT.2015.10.028.

[39] H. Monzón, M.A. Laguna-Bercero, The influence of reduction conditions on a Ni-YSZ SOFC anode microstructure and evolution, ECS Trans. 68 (1) (2015) 1229–1235, https://doi.org/10.1149/06801.1229ECST.

[40] R. Straubinger, A. Beyer, K. Volz, Preparation and loading process of single crystalline samples into a gas environmental cell holder for in situ atomic resolution scanning transmission electron microscopic observation, Microsc. Microanal. 22 (3) (2016) 515–519, https://doi.org/10.1017/S1431927616000593.

[41] M. Hammad Fawey, V.S.K. Chakravadhanula, M.A. Reddy, et al., In situ TEM studies of micron-sized all-solid-state fluoride ion batteries: preparation, prospects, and challenges, Microsc. Res. Tech. 79 (7) (2016) 615–624, https://doi.org/10.1002/JEMT.22675.

[42] S. Gorji, A. Kashiwar, L.S. Mantha, et al., Nanowire facilitated transfer of sensitive TEM samples in a FIB, Ultramicroscopy 219 (2020), https://doi.org/10.1016/J.ULTRAMIC.2020.113075.

[43] A. Hauch, K. Brodersen, M. Chen, M.B. Mogensen, Ni/YSZ electrodes structures optimized for increased electrolysis performance and durability, Solid State Ionics 293 (2016) 27–36, https://doi.org/10.1016/J.SSI.2016.06.003.
[44] D. Sarantaridis, A. Atkinson, Redox cycling of Ni-based solid oxide fuel cell anodes: a review, Fuel Cell. 7 (3) (2007) 246–258, https://doi.org/10.1002/FUCE.200600028.
[45] K.V. Hansen, T. Jacobsen, K. Thyden, Y. Wu, M.B. Mogensen, In situ surface reduction of a NiO-YSZ-alumina composite using scanning probe microscopy, J. Solid State Electrochem. 18 (7) (2014) 1869–1878, https://doi.org/10.1007/S10008-014-2428-9/FIGURES/6.
[46] R.A. Vilá, W. Huang, Y. Cui, Nickel impurities in the solid-electrolyte interphase of lithium-metal anodes revealed by cryogenic electron microscopy, Cell Rep. Phys. Sci. 1 (9) (2020) 100188, https://doi.org/10.1016/J.XCRP.2020.100188.
[47] D. Klotz, A. Weber, E. Ivers-Tiffée, Practical guidelines for reliable electrochemical characterization of solid oxide fuel cells, Electrochim. Acta 227 (2017) 110–126, https://doi.org/10.1016/J.ELECTACTA.2016.12.148.
[48] I. Utke, S. Moshkalev, P. Russell, Nanofabrication Using Focused Ion and Electron Beams, Oxford University Press, 2011.
[49] T. Hidayat, M.A. Rhamdhani, E. Jak, P.C. Hayes, Investigation of nickel product structures developed during the gaseous reduction of solid nickel oxide, Metall. Mater. Trans. B 40 (4) (2009) 462–473, https://doi.org/10.1007/S11663-009-9247-X.
[50] J.A. Rodriguez, J.C. Hanson, A.I. Frenkel, J.Y. Kim, M. Pérez, Experimental and theoretical studies on the reaction of H2 with NiO: role of O vacancies and mechanism for oxide reduction, J. Am. Chem. Soc. 124 (2) (2002) 346–354, https://doi.org/10.1021/JA0121080.
[51] S. Li, L. Yang, J. Christudasjustus, et al., Selective atomic sieving across metal/oxide interface for super-oxidation resistance, Nat. Commun. 15 (1) (2024 15:1. 2024) 1–10, https://doi.org/10.1038/s41467-024-50576-7.
[52] S. De Angelis, P.S. Jørgensen, V. Esposito, et al., Ex-situ tracking solid oxide cell electrode microstructural evolution in a redox cycle by high resolution ptychographic nanotomography, J. Power Sources 360 (2017) 520–527, https://doi.org/10.1016/J.JPOWSOUR.2017.06.035.
[53] P. Fortier, G. Palumbo, G. Brucej, W. Miller, K. Aust, Triple line energy determination by scanning tunneling microscopy, Scripta Metall. Mater. 25 (1991) 177–182, 25:177-182.
[54] K. Syed, N.B. Motley, W.J. Bowman, Heterointerface and grain boundary energies, and their influence on microstructure in multiphase ceramics, Acta Mater. 227 (2022) 117685, https://doi.org/10.1016/J.ACTAMAT.2022.117685.
[55] S.L. Thomas, C. Wei, J. Han, Y. Xiang, D.J. Srolovitz, Disconnection description of triple-junction motion, Proc. Natl. Acad. Sci. U.S.A. 116 (18) (2019) 8756–8765, https://doi.org/10.1073/PNAS.1820789116.
[56] J.A. Rodriguez, J.C. Hanson, A.I. Frenkel, J.Y. Kim, M. Pé Rez, Experimental and Theoretical Studies on the Reaction of H 2 with NiO: Role of O Vacancies and Mechanism for Oxide Reduction, 2002, https://doi.org/10.1021/ja0121080. Published online.
[57] X. Li, X. Guan, Z. Jia, P. Chen, C. Fan, F. Shi, Twin-related grain boundary engineering and its influence on mechanical properties of face-centered cubic metals: a review, Metals 2023 13 (2023) 155, https://doi.org/10.3390/MET13010155, 13(1):155.
[58] I. Bakonyi, V.A. Isnaini, T. Kolonits, et al., The specific grain-boundary electrical resistivity of Ni, Phil. Mag. 99 (9) (2019) 1139–1162, https://doi.org/10.1080/14786435.2019.1580399.
[59] H. Luo, W. Lu, X. Fang, D. Ponge, Z. Li, D. Raabe, Beating hydrogen with its own weapon: nano-twin gradients enhance embrittlement resistance of a high-entropy alloy, Mater. Today 21 (10) (2018) 1003–1009, https://doi.org/10.1016/J.MATTOD.2018.07.015.
[60] S. Mahajan, G.Y. Chin, Formation of deformation twins in f.c.c. crystals, Acta Metall. 21 (10) (1973) 1353–1363, https://doi.org/10.1016/0001-6160(73)90085-0.
[61] R. Bhattacharyya, K. Bhanja, S. Mohan, Mathematical analysis of reduction of copper oxide pellets by hydrogen using the shrinking core model, Fusion Eng. Des. 100 (2015) 560–564, https://doi.org/10.1016/J.FUSENGDES.2015.08.005.
[62] Z. Yang, L. Wang, J.A. Dhas, et al., Guided anisotropic oxygen transport in vacancy ordered oxides, Nat. Commun. 14 (1) (2023) 1–9, https://doi.org/10.1038/s41467-023-40746-4, 14:1. 2023.
[63] M.R. Pillai, Y. Jiang, N. Mansourian, et al., Microstructure and long-term stability of Ni–YSZ anode supported fuel cells: a review, Mater. Futures 1 (4) (2022) 042101, https://doi.org/10.1088/2752-5724/AC88E7.